RESEARCH ARTICLE

On the effects of landscape configuration on summer diurnal temperatures in urban residential areas: application in Phoenix, AZ

Yiannis KAMARIANAKIS (✉)[1], Xiaoxiao LI[2], B. L. TURNER II[2,3,4], Anthony J. BRAZEL[2,4]

1 School of Mathematical and Statistical Sciences, Arizona State University, Tempe AZ 85287, USA
2 School of Geographical Sciences and Urban Planning, Arizona State University, Tempe AZ 85298, USA
3 School of Sustainability, Arizona State University, Tempe AZ 85298, USA
4 Global Institute of Sustainability, Arizona State University, Tempe AZ 85287, USA

Abstract The impacts of land-cover composition on urban temperatures, including temperature extremes, are well documented. Much less attention has been devoted to the consequences of land-cover configuration, most of which addresses land surface temperatures. This study explores the role of both composition and configuration—or land system architecture—of residential neighborhoods in the Phoenix metropolitan area, on near-surface air temperature. It addresses two-dimensional, spatial attributes of buildings, impervious surfaces, bare soil/rock, vegetation and the "urbanscape" at large, from 50 m to 550 m at 100 m increments, for a representative 30-day high sun period. Linear mixed-effects models evaluate the significance of land system architecture metrics at different spatial aggregation levels. The results indicate that, controlling for land-cover composition and geographical variables, land-cover configuration, specifically the fractal dimension of buildings, is significantly associated with near-surface temperatures. In addition, statistically significant predictors related to composition and configuration appear to depend on the adopted level of spatial aggregation.

Keywords land system architecture, urban heat island effect, linear mixed-effects models, near-surface air temperature, land-cover configuration

1 Introduction

Urban and regional "metroplex" heat island (UHI) effects are expected to grow in intensity and aerial extent with increasing global urbanization and climate warming (e.g., Georgescu et al., 2014; Wang and Akbari, 2016). These changes, in turn, hold numerous consequences for human health, energy and water consumption, and biotic diversity (e.g., Akbari et al., 2001; Guhathakurta and Gober, 2010; Faeth et al., 2011; Hondula et al., 2013), amplifying attention to the mitigation of extreme heat, especially among cities in warm climates. Redesigning the composition and configuration of "cityscapes" and urban-rural landscapes—variously labeled the land system architecture (Turner et al., 2013), landscape mosaics (Forman, 1990), or urban morphology/geometry (Stewart and Oke, 2012)—constitute a mitigation option. A variety of research demonstrates the significance of land composition on urban temperature, including land surface and within and above the urban boundary layer temperatures (e.g., Cermak et al., 2017). For example, the concentration of buildings and impervious surfaces amplifies temperatures (e.g., Stone and Rodgers, 2001; Nichol et al., 2009; Krüger et al., 2011; Yang et al., 2011). In contrast, cool or green roofs (Gill et al., 2007; Jacobson and Ten Hoeve, 2012; Georgescu et al., 2014) and the vegetation or green space fraction (e.g., Akbari et al., 2001; Wong and Yu, 2005; Bowler et al., 2010; Li et al., 2011; Zhou et al., 2011; Akbari and Matthews, 2012; Li et al., 2012) attenuate temperature extremes. In addition to these land-cover composition characteristics, evidence mounts that the configuration of the land system—the pattern and shape of individual land covers or their mosaics—affects urban temperatures as well (Xiao et al., 2007; Zhou et al., 2011; Li et al., 2012, 2016, 2017; Maimaitiyiming et al., 2014; Huang and Cadenasso, 2016).

The heat vulnerability of neighborhoods is a significant concern for the metropolitan area of Phoenix, Arizona (USA), where maximum summer daytime temperatures

routinely exceed 40°C in summer and have reached 50°C (122°F) (Middel et al., 2012). As such, considerable local climate and UHI research on the metropolitan area has been undertaken (e.g., Baker et al., 2002; Grimmond, 2007; Jenerette et al., 2011, 2016; Chow et al., 2012), largely focused on land surface temperature and the composition of land covers (Harlan et al., 2006; Gober et al., 2010; Grossman-Clarke et al., 2010; Myint et al., 2010; Li et al., 2011; Chow and Brazel, 2012; Connors et al., 2013; Myint et al., 2013). These efforts, consistent with research elsewhere, indicate that the amount of land cover, foremost that of impervious surfaces, vegetation, and bare soil, affect daytime and nighttime land surface temperatures. Increasingly, however, the role of the configuration of land units, in tandem with their composition, on land surface temperatures draws attention. This orientation, referred to here as land system architecture, examines the influence on temperature created by the pattern and shape of land covers at fine-grain, spatial resolutions. It treats multiple land covers in more compositional detail than urban morphological approaches in urban climatology, but to date, lacks the vertical dimensions of the composition in morphological approaches that permit assessments of turbulent sensible and latent heat flux (Turner, 2016). Investigations falling within the umbrella of land architecture reveal that compactly shaped clustering of certain land covers, from the sub-parcel to aggregate levels of assessment, prove to be as important for land surface temperature as the overall amount of space devoted to those covers (Myint et al., 2015, 2016; Li et al., 2016, 2017; Zhang et al., 2017).

Less attention has been given to the role of land system architecture at large (as opposed to specific objects, such as building and trees) on temperature within the urban boundary layer (i.e., near-ground or near-surface temperature > 2 m above the land surface but below the rooftop). While nighttime temperatures in this layer may mirror somewhat those of the land surface, significant differences commonly exist during the day (Voogt and Oke, 2003), demonstrated for Phoenix, AZ (Stoll and Brazel, 1992). Middel et al. (2014) identified urban form, including that of the land system, as having a large impact on daytime above-ground temperature extremes in the Phoenix metro-area. In addition, Myint et al. (2010) and Lindén (2011) examined the role of land-cover fractions (i.e., land-cover pattern) on selected near-ground station air temperatures for the Phoenix area and Ouagadougou, Burkina Faso (semi-arid steppe climate of the Sahel), respectively. For the most part, however, the poor spatial match between near-ground temperature data and the complex and heterogeneous character of urban land-cover data impedes examinations of the details of fine-resolution, land-cover configuration, both pattern and shape.

In-situ weather stations provide near-ground temperatures with fine temporal resolution that accurately reflect the extreme temperatures (Myint et al., 2010; Chow et al.,

2011, 2014; Chow and Brazel, 2012). The small number and large spacing of weather stations, however, constrain the utility of these data for the examination of land architecture-temperature relationships in highly heterogeneous urban land systems. Several past studies have used point weather station sites (at heights of 2 m), adopting the World Meteorological Organization's urban area siting criteria (e.g., Oke, 2006, typically 500 m around a site), but have not focused on land-cover configuration per se. The location of urban flux towers (above the urban canopy) provides data to calculate or estimate source regions of fluxes based on wind rose and stability criteria. The size of area for which temperatures is generated vary, however, owing to the height of the sensors, commonly on towers 30 m above ground level or on top of buildings. As such, the size of the temperature area, including the temperature estimates generated from the tower measurements, are typically larger than the parcel on which the towers are located, registering the aggregate results from multiple land covers.

This study expands the land system architecture research on the Phoenix metropolitan area by linking fine-resolution (1 m) land-cover data to near-ground temperature (within the urban canopy) data, recorded on individual parcels across 44 residential areas. It seeks to determine if and how land composition and configuration (i.e., land architecture) affect daytime and nighttime near-ground temperature among single-family residences in the metroplex and at what spatial scales the relationships, if any, are more significant.

Standardized buffers of 50 m to 550 m in 100 m intervals around residential weather stations provide the base areas of assessment of the near-ground temperature data, matched by land-cover data derived from 1 m NAIP 4-band imagery. Following the work on land architecture and land surface temperature in the Phoenix metropolitan area (above), our working hypothesis projects fine-resolution land-cover configuration, in addition to land composition, affects near surface temperatures, and does so differentially at different times of the day. While the evidence mounts for the roles of land-cover configuration — for instance, increasing patch density of compactly shaped vegetation generating significant cooling effects in arid environments — the depth of this understanding relative to configuration metrics across varied land covers is sparse, especially applied directly to near-ground temperature.

2   Data and methods

2.1   Study area

The central Arizona-Phoenix metropolitan area (Fig. 1) covers more than 7600 km² of the northern Sonoran Desert in Maricopa County (Wentz et al., 2006; Connors et al., 2013). The area experiences a subtropical desert climate
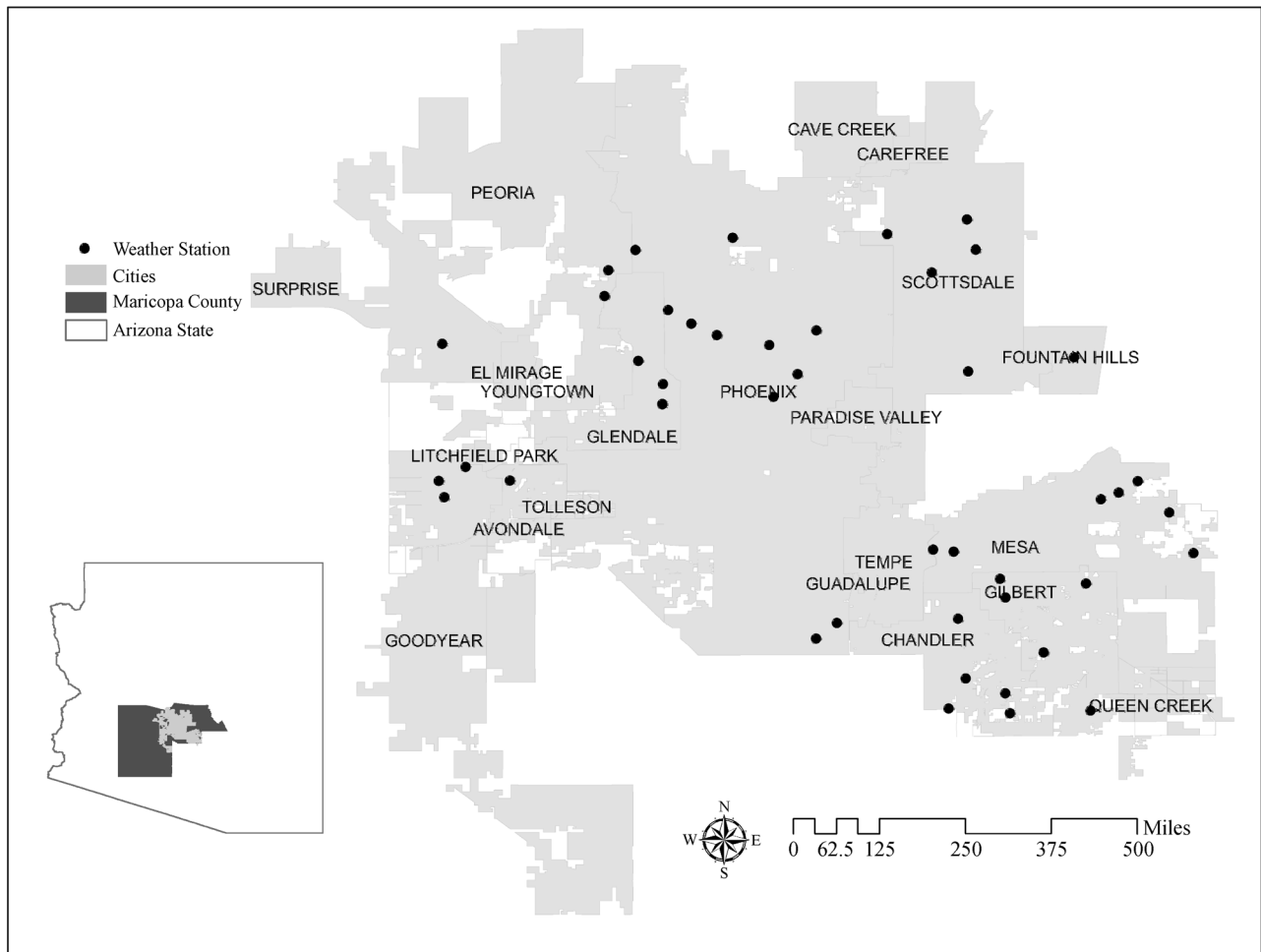
Fig. 1 The Phoenix, AZ, metropolitan area. The boundaries and names identify the cities in the metroplex. The residential study sites correspond to the 44 selected weather stations.

with hot summers and warm winters. Phoenix and its surrounding cities have witnessed dramatic urban sprawl, especially since the middle of the last century. A large majority of this sprawl constitutes residential housing conforming to the LCZ6 zone defined by Stewart et al. (2014). The resulting residential neighborhoods comprise openly arranged buildings, in this case overwhelmingly one story creating uniformity in their vertical dimension, with adjacent trees and other vegetation rarely exceeding the height of the buildings.

This growth and desert location increases human exposure to extreme temperatures (Chow and Svoma, 2011; Chow et al., 2012). For example, the average June maximum air temperature is 40°C (104°F) and minimum, 22.7°C (72.9°F). Brazel et al. (2000) and Grossman-Clarke et al. (2010) have shown an emerging heat island within the metro area since the 1970s with magnitude of some 5°C–10°C, the largest distinction with the ambient, rural temperature occurring at night. Recent assessments, however, indicate that Phoenix metro-area neighborhoods

are 2°C–3°C cooler than urban surfaces (e.g., Phoenix airport site, the central business district) all day; 2°C–6°C cooler during the day than other sites, but 2°C–8°C warmer at night than open city park, rural agriculture and desert locales (e.g., Li et al., 2017).

2.2 Remotely sensed data

The National Agricultural Imagery Program (NAIP) four-band (red, green, blue, and near inferred band) orthophoto mosaic data were used with an object based image analysis (OBIA) to produce a 1 m resolution land-cover map for Phoenix (Fig. 1) (Li et al., 2014). The original NAIP imagery comprises 59 digital ortho quarter quad tiles (DOQQs) covering 3.75 by 3.75 minute quarter quad-rangle with a 300 m buffer, 90% of which were taken during June 6–10, 7% on August 15, and 3% on September 9, 2010. The imagery was pre-processed with pixel-based spectral transformation including principal component analysis (PCA), RGB (red, green, and blue) to HIS (hue,

intensity, and saturation) color space values, and spatial enhancement, including convolution and morphological functions. The transformed data and original four-band aerial photos were stacked together as input for object-based classification. Expert-knowledge decision rules guided the OBIA method, assisted by cadastral parcel vector data.

Using a hierarchical image object network, four types of segmentation (multi-resolution, multi-threshold, Quadtree based, and chessboard segmentation) and classification algorithms were grouped into rule sets for characteristics selection using spectral, spatial, geometrical, and contextual information and image object identification. Due to the large volume of data, each of the 59 DOQQs were executed with OBIA rule sets using the tilting analysis in the workspace of Definiens software. Morphological operators (erode to perform focal minimum analysis and dilate to perform focal maximum analysis), used before and after the OBIA and post-classification editing, further improved the land-cover mapping accuracy. The Mosaic-Pro module in ERDAS software mosaicked the 59 DOQQs into one image using the "Most NidarSeamline" generation method to fill the gaps between the DOQQs.

Twelve land-cover classes were identified, six of which are employed in this study — building, road, bare soil/rock, tree/shrub and grass — that comprise the overwhelming area of residential parcels — and swimming pools (i.e., water), which account for less than 1% of residential parcels. These six land-covers generate producer and user accuracies of 86.52% to 98.04% and 88.35% to 98.04%, respectively. Swimming pools do not exist on all residential parcels: for this reason, pools were not included in the set of explanatory variables of the predictive models, although the presence of pools was a statistically significant predictor for both daytime and nighttime land surface temperatures in previous studies (Li et al., 2017). Driveways and bare soil/rock constitute one class because of the similarities in their signal signatures.

2.3 Air temperature data

WeatherUnderground, which includes MesoWest stations, provided 3-hourly air temperature and wind data from 44 automated weather stations located in residential areas of the metropolitan region. A larger number of stations recording data and covering a greater range of single-family residential neighborhoods exists for 2011 than for 2010, prompting the use of the 2011 weather data applied to the 2010 land-cover data.

Measurements correspond to a pre-monsoon period (June 1–30, 2011) which were exemplary of summer conditions (high sun) not overly affected by rainfall, clouds, or strong winds (Brazel et al., 2007): the air mass was dry tropical, which is experienced 70% of the time in June. Such conditions are highly suitable for air temperature assessments related to land architecture and are difficult to encounter for monthly periods during other seasons in the Phoenix area. For June 2011, our sample period, 27 of 30 days (90% of time) were classified as dry tropical, a stable atmospheric state in which minimal disturbance, if any, exists between land surface (i.e., land cover) and near ground temperatures above that surface. For the most part, wind speeds at study sites were very low at night and not more than 2–2.5 m/s during daytime. Fast et al. (2005) advocate that winds in this range lead to microclimate temperature variability and heat island conditions. The analysis that follows employs air temperature data that correspond to wind speeds less than 6 m/s; removed from analysis were observed temperatures associated with stronger winds.

2.4 Land architecture metric calculation

Metrics indicative of land-cover composition and configuration were calculated using FRAGSTATS 4.2 (McGarigal et al., 2012) for individual land-cover classes (e.g., vegetation) and for their aggregate or landscape condition. Buffer zones around each weather station with radii ranging from 50 m to 550 m, at 100 m intervals served as the spatial support of calculation. Five metrics were computed for each land-cover type: percent of land-cover type (PLAND) for land composition, and patch density (PD), edge density (ED), landscape shape index (LSI) and fractal dimension index (FRAC) for land configuration (Table 1). PLAND measures the fraction of patches of each land-cover type within a unit, while the spatial configuration metrics characterize the shape complexity and spatial distribution of patches in the unit (Table 1). Two additional configuration metrics, namely Contagion (CONTAG) and Shannon's diversity index (SHDI), capture the aggregated architecture of land patches (Table 1). Assessments of land surface temperature commonly employ these five metrics, which capture important dimensions of configuration, both pattern and shape; many other FRAGSTATS metrics overlap the dimensions generated by the five employed and were not employed.

The temperature data and land architecture metrics corresponding to the buffer zones for each station were matched. Figure 2 presents three samples of weather stations (KAZCHAND23 in the city of Chandler, KAZGLEND17 in the city of Glendale, and KAZPHOEN110 in the city of Phoenix) with different spatial scale buffers. These three samples represent mesic (lawn turf), xeric (desert-scape), and in-between mesic-xeric residential neighborhoods respectively.

2.5 Statistical analysis

Linear mixed-effects models (LMM) were developed to assess the significance of land architecture metrics. In the exploratory stage of the analysis temperatures measured at location s, denoted by T_s, were modelled using two site-

Table 1 Land architecture metrics

Metric/abbreviation	Description	Class specific metrics	Aggregated parcel metrics
Percent cover of a land-cover class/ PLAND	Proportion of the land-cover type (patch type) on the unit landscape plot ($0 < \text{PLAND} \leqslant 100$)	PLAND of Building, Soil, Soil, Tree/Shrub, Grass	N/A
Patch density/PD	Number of patches/ha (> 0, determined by grain or pixel size)	PD of Building, Soil, Soil, Tree/Shrub, Grass	PD
Edge Density/ED	Total length of edges for all patches/ha ($\geqslant 0$, where 0 refers to a landscape composed of one patch)	ED of Building, Soil, Soil, Tree/Shrub, Grass	ED
Landscape Shape index/LSI	Total length of all patch edges divided by the minimum possible length of the area of the unit landscape plot ($\geqslant 1$, where the greater the LSI above 1 the more the shape deviates from a compact shape, i.e., a square)	LSI of Building, Soil, Soil, Tree/Shrub, Grass	LSI
Fractal dimension/ FRAC	A measure of shape complexity by calculating the departure of the patch from its Euclidean geometry ($1 \leqslant \text{FRAC} \leqslant 2$, where 1 corresponds to very simple shapes and 2 to extremely complex shapes)	FRAC of Building, Soil, Soil, Tree/Shrub, Grass	FRAC
Contagion/CONTAG	A measure of adjacency of patches ($0 < \text{CONTAG} \leqslant 100$, where patches are maximally disaggregated and dispersed when the values are small; 100 is the reverse)	N/A	CONTAG
Shannon's diversity index/SHDI	A measure of the diversity of patches (0 is a landscape with 1 patch)	N/A	SHDI

specific regression models that captured the diurnal patterns and the increasing trend of temperatures in June. Both models were based on linear trend terms; the first encapsulated diurnal patterns using sinusoidal terms:

$$\hat{T}_s(t) = \beta_{0,s} + \beta_{1,s}\sin\left(^{2\pi h(t)}/24\right)\beta_{2,s}\cos\left(^{2\pi h(t)}/24\right)$$

$$+\beta_{3,s}d(t). \tag{1}$$

In Eq. (1), $\hat{T}_s(t)$ denotes predicted temperatures at site s, during the $h(t)^{th}$ hour of the $d(t)^{th}$ day in the sample. The slopes $\beta_{3,s}$ capture site-specific linear trends and the diurnal patterns are expressed by the predictors that correspond to $\beta_{1,s}$ and $\beta_{2,s}$. The four site-specific coefficients $\beta_{0,s}$, $\beta_{1,s}$, $\beta_{2,s}$, $\beta_{3,s}$ were estimated by least squares.

The second specification was more flexible (and less parsimonious) as it represented diurnal profiles based on dummy variables:

$$\hat{T}_s(t) = \sum_{i=1}^{8} \left(\beta_{i,s}I\left(h(t) = 3i\right)\right) + \beta_{9,s}d(t). \tag{2}$$

Eq. (2) is based on the characteristic function with $I(h(t) = 3i) = 1$ if $h(t) = 3i$ and $I\left(h(t) = 3i\right) = 0$ if $h(t) \neq 3i$; as i increases the dummy variables correspond to different time periods. The model presented in Eq. (2) provided superior predictive power relative to Eq. (1). Hence, subsequent analyses were based on that specification. Correlations between coefficients that capture location-specific trends and diurnal profiles in Eq. (2) with land architecture metrics and geographical coordinates were calculated for different (spatial) aggregation intervals. This part of the exploratory analysis guided the model building

procedure of LMM.

LMM are generalizations of site-specific regression models, which may summarize temperature dynamics observed at multiple locations. Mixed-effects models contain fixed and random effects: fixed effects denote 'average' model parameters whereas random effects represent site-specific deviations from 'average' dynamics. LMM can be used for site-specific inference and forecasting when estimates at both levels (fixed and random effects) are taken into account. LMM also predict temperatures at sites not included in model estimation, based solely on the coefficients that correspond to fixed effects; such predictions apply to sites for which model estimation is infeasible due to insufficient data.

A general LMM based on Eq. (2), henceforth called LMM_0, is formulated as:

$$T_s(t) = \sum_{i=1}^{8}(\beta_i + b_{i,s})I(h(t) = 3i) + (\beta_9 + b_{9,s})d(t) + \varepsilon_s(t)$$

$$b_{i,s} \sim N(0, \psi_i^2), Cov(b_{i,s}, b_{j,s}) = \psi_{i,j}, i, j = 1, ..., 9, i \neq j$$

$$\varepsilon_s(t) \sim N(0, \sigma^2 \lambda_s), Cov(\varepsilon_s(t), \varepsilon_s(t-k)) = \sigma^2 \lambda_{sk}. \tag{3}$$

The fixed effects coefficients β_i constitute the mean values of the diurnal profiles and the linear trend parameters across all measurement sites. Random effects $b_{i,s}$, $i = 1, 2, ..., 9$ (with s denoting measurement site) express site-specific deviations. Random effects are assumed to follow a multivariate normal distribution with variances ψ_i^2 and covariances $\psi_{i,j}$; ψ will denote the resulting covariance matrix. The site-specific error terms

ε_s, are assumed normally distributed and independent of the random effects. The covariance structure of the error terms aims to account for remaining serial correlation: the λ_{sk} (k denotes time lags) are derived using an autoregressive specification AR(p).

The null model presented in Eq. (3) can be augmented so that part of the variability of the random effects is explained by site-specific environmental and geographical characteristics. For instance, the specification shown below, hereafter LMM$_{geog}$, contains n_1 additional predictors, denoted by x, which correspond to geographical coordinates of measurement sites:

$$T_s(t) = \sum_{i=1}^{8}(\beta_i + b_{i,s})I(h(t) = 3i) + (\beta_9 + b_{9,s})d(t)$$
$$+ \sum_{l=1}^{n_1}\gamma_l x_{l,s} + \varepsilon_s(t)$$

$$b_{i,s} \sim N(0, \psi_i^2), Cov(b_{i,s}, b_{j,s}) = \psi_{i,j}, i,j = 1,2,...,9, i \neq j,$$

$$\varepsilon_s(t) \sim N(0, \sigma^2\lambda_s), Cov(\varepsilon_s(t), \varepsilon_s(t-k)) = \sigma^2\lambda_{sk}, \qquad (4)$$

LMM$_{geog}$ can be further augmented to include land architecture metrics. For spatially aggregated land architecture metrics computed using radius r, with $r = 50,150,...,550$ m, LMM$_r$ contains $n_2(r)$ additional predictors, denoted by $z^{(r)}$:

$$T_s(t) = \sum_{i=1}^{8}(\beta_i + b_{i,s})I(h(t) = 3i) + (\beta_9 + b_{9,s})d(t)$$
$$+ \sum_{l=1}^{n_1}\gamma_l x_{l,s} + \sum_{m=1}^{n_2(r)}\delta_m z_{m,s}^{(r)} + \varepsilon_s(t)$$

$$b_{i,s} \sim N(0, \psi_i^2), Cov(b_{i,s}, b_{j,s}) = \psi_{i,j}, i,j = 1,...,9, i \neq j,$$

$$\varepsilon_s(t) \sim N(0, \sigma^2\lambda_s), Cov(\varepsilon_s(t), \varepsilon_s(t-k)) = \sigma^2\lambda_{sk}, \qquad (5)$$

where $n_2(r)$ represents the number of statistically significant land architecture (composition and configuration) metrics for radius r. A specification of particular interest is based on statistically significant land architecture metrics for all available aggregation radii. This model is designated by LMM$_{comb}$ in what follows.

The protocol presented in Zuur et al. (2009) guided the model building procedure for the LMM presented in Eqs. (3)–(5). First a regression model was estimated using all possible predictors after excluding predictors that caused instabilities due to multicollinearity. A backward stepwise procedure based on variance inflation factor criterion (VIF; James et al., 2013) removed collinear predictors:

$$VIF_q = \frac{1}{1 - R_q^2}. \qquad (6)$$

VIF for predictor q was obtained using the coefficient of determination (R^2) from the regression of that predictor against all other explanatory variables. VIFs were calculated for each predictor; that with the highest VIF was removed at each step of the backward procedure, provided that the condition $VIF_q > 20$ was satisfied.

The next step in the model building procedure examined which of the predictors needed random effects to account for between-site variability and which could be treated as purely fixed effects. For instance, if variability of slopes $b_{s,9}$ is not significant across measurement locations, the temporal trends are modeled using solely β_9; this finding implies common trends across measurement sites (in accordance with prior expectations). Simplified versions of the general model, with fewer random effects and block-diagonal covariance structures were evaluated using likelihood ratio tests. [These tests compare nested models estimated by restricted maximum likelihood as detailed in Pinheiro and Bates (2009)]. Once the optimal random structure was found, the optimal structure for the fixed effects was decided using likelihood ratio tests. Finally, for the error terms $\varepsilon_s(t)$, a backward stepwise procedure evaluated AR(p) specifications with maximum order $p = 4$.

Fixed-effects represent 'average' model parameters whereas random-effects denote site-specific deviations from 'average' dynamics. In the next section we report estimated coefficients on standardized variables. These coefficients represent the effect of a standard deviation change for a predictor, keeping the other predictors fixed, and allow us to evaluate the relative significance of the explanatory variables. Stepwise model building for LMM$_r$ and LMM$_{comb}$ prioritized geographic and land composition variables: an explanatory variable related to land configuration was included in the final specifications, only if it provided significant additional explanatory power relative to predictors that represent geographic characteristics and land composition.

Mixed-effects models can be used to predict near-ground air temperatures at measurement sites not included in the original sample; hence, LMM$_0$, LMM$_{geog}$, LMM$_r$ and LMM$_{comb}$ can be evaluated in terms of their generalization ability by leave-one-site-out cross-validation. Thus the significance of land architecture metrics included in LMM$_r$ was assessed by comparing the generalization ability of LMM$_r$ relative to LMM$_0$ and LMM$_{geog}$. The accuracy metrics, reported in the next section, include: 1) mean error (ME), a measure of bias; 2) median absolute error (MedAE); and 3) root mean square error (RMSE).

3   Results and discussion

3.1   Exploratory analysis

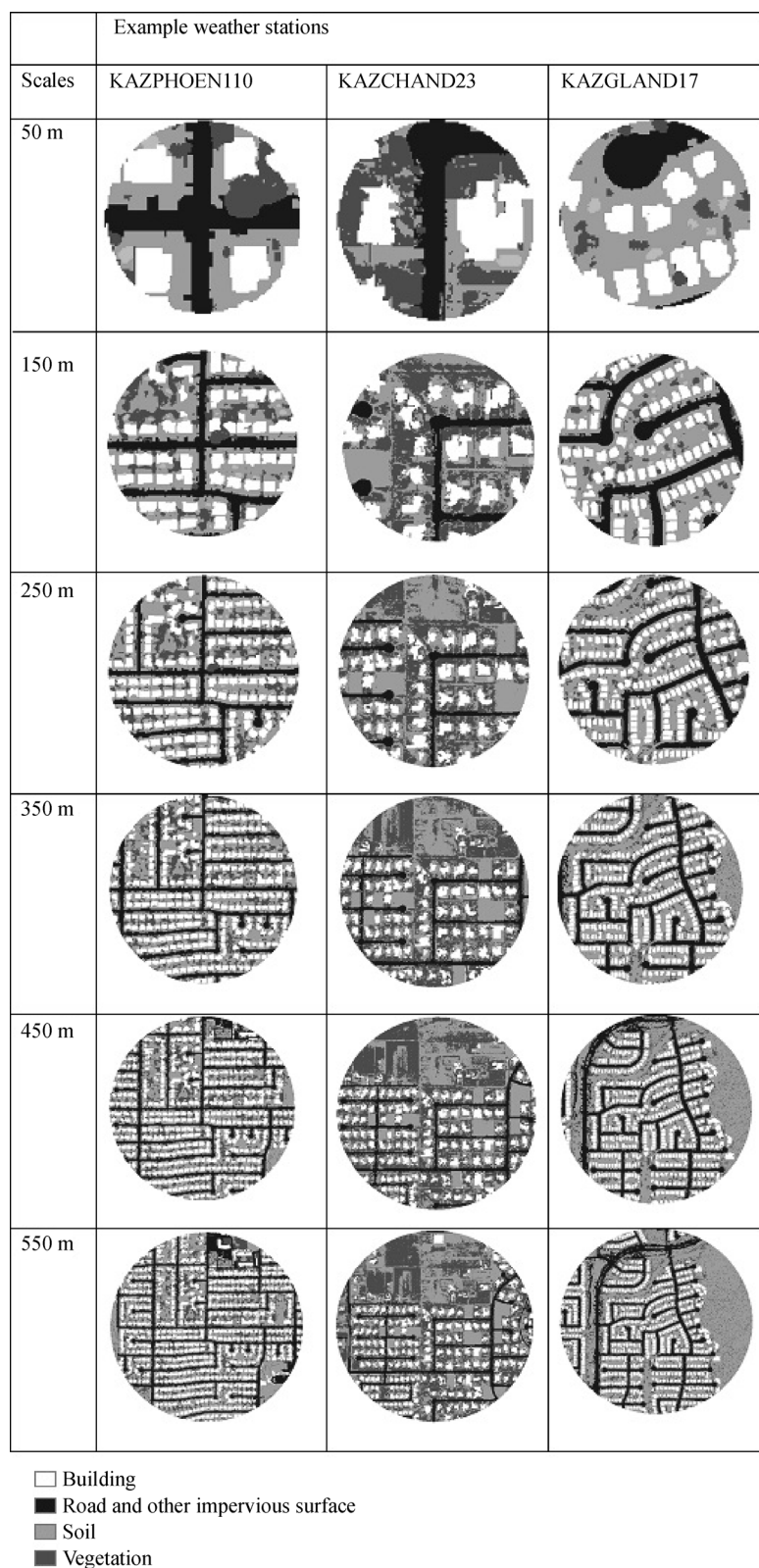Figure 3 shows the diurnal patterns of the analyzed near-ground temperatures, with large differences between

	Example weather stations		
Scales	KAZPHOEN110	KAZCHAND23	KAZGLAND17
50 m			
150 m			
250 m			
350 m			
450 m			
550 m			

☐ Building
■ Road and other impervious surface
▨ Soil
■ Vegetation

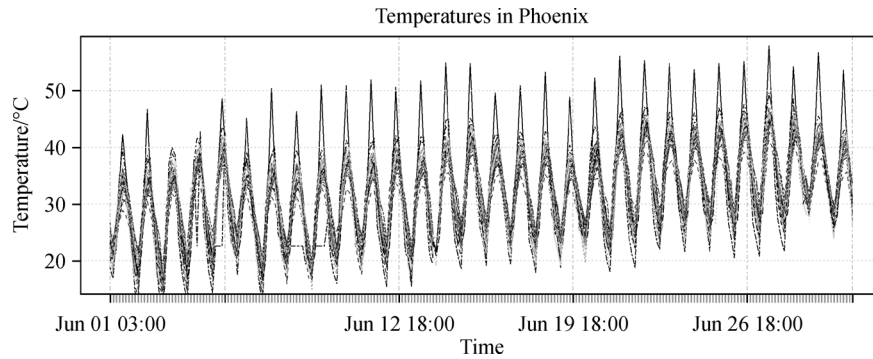**Fig. 2**   Selected samples for buffer zones at different scales.

Fig. 3 Air temperatures observed in 44 stations in the Phoenix metroplex during June 2011.

daytime and nighttime, in some cases exceeding 15°C. The increasing trend of temperatures in June is apparent. De-trended temperatures, derived by subtracting site-specific linear trends from the original measurements, do not suggest substantial differences in temperature variability for nighttime and daytime (Fig. 4). Winds minimally affected the temperature: measurements confirm low wind speeds typical of dry tropical clear days in summer (Fig. 4). Inspection of the wind direction data for all sites revealed a pattern representative of June, with westerly and southerly flow off the deserts toward Phoenix (Stewart et al., 2002) almost all day, with only a couple of sites near the southeast mountains experiencing some nighttime reversals of wind that transitioned to southwest in the morning.

On average soil occupies 38.5% of the land surface around the measurement stations. Variability for different levels of spatial aggregation was minimal compared to variability across measurement sites. The observed minima of the percentage of soil across measurement sites were close to 17% and the observed maxima, close to 73%. Similar findings (Fig. 5) hold for the average percentages of buildings (18%), roads (20%), trees/shrubs (12%), and grass (9.2%). As noted above, pools account for the (small) remaining percentage of land and were not included in the statistical models. With regard to shape complexity, it is worth noting that, on average, the fractal dimension of buildings was close to 1.1. This figure is lower (revealing less complex shapes) relative to the remaining land-cover types, for which fractal dimensions ranged from 1.2 to 1.3.

Figure 6 shows the coefficients of determination for site-specific regressions presented in Eq. (1) and Eq. (2). The less parsimonious specification based on dummy variables explained at least 85%, and at most 96%, of the variability of near-ground air temperatures. Eq. (1) on the other hand, explained at least 82%, and at most 94%, of that variability. Linear trends were deemed adequate given that the magnitudes of the coefficients of determination are very close to unity for the regressions in Eq. (2). The estimated linear trends were statistically significant for all measurement sites and imply an expected daily increase of near ground temperatures in June that ranges from 0.25°C to 0.45°C (Fig. 6).

Land architecture metrics that strongly correlate with the slopes of the linear trends and the dummies that capture diurnal profiles in Eq. (2) are expected to explain part of the variability of the site-specific random effects in the mixed-effects models, enhancing the generalization ability of LMM. In accordance with prior expectations, elevation, which ranges from 91 to 257 m (300 to 845 ft) above mean sea level for the examined stations, is strongly associated with the dummies that correspond to afternoon temperatures. It is worth noting that the fractal dimension of buildings (FRAC1_50 – FRAC1_550) and the patch density of soil (PD3_50 – PD3_550) are consistently negatively associated with nighttime temperatures for all examined levels of spatial aggregation (Fig. 7). In contrast, the percentage of buildings is, in general, positively associated with nighttime temperatures, whereas the percentage of trees and shrubs is negatively correlated with nighttime temperatures for all aggregation levels.

3.2 Mixed-effects models

Tables 2–4 present nine mixed-effects models and their evaluation based on leave-one-measurement-site-out cross-validation. All quantitative variables were standardized, so that fixed-effects coefficients represent the estimated effect (on air temperatures) of a standard deviation change on the levels of the corresponding predictor, keeping all other predictors fixed (for strongly correlated predictors this may not be possible in reality). In contrast with the terms that capture the diurnal profiles, linear trends do not vary significantly across measurement sites in all mixed effects models: a common fixed-effect term is sufficient. The fixed-effects terms of LMM_0, based solely on temporal information, are in conformity with the diurnal patterns observed in Fig. 4. Elevation is the only statistically significant geographical covariate in LMM_{geog}. As expected, it exerts a negative effect on air temperatures, and its addition results in improved generalization ability relative to LMM_0 in terms of MedAE and RMSE (Table 2).

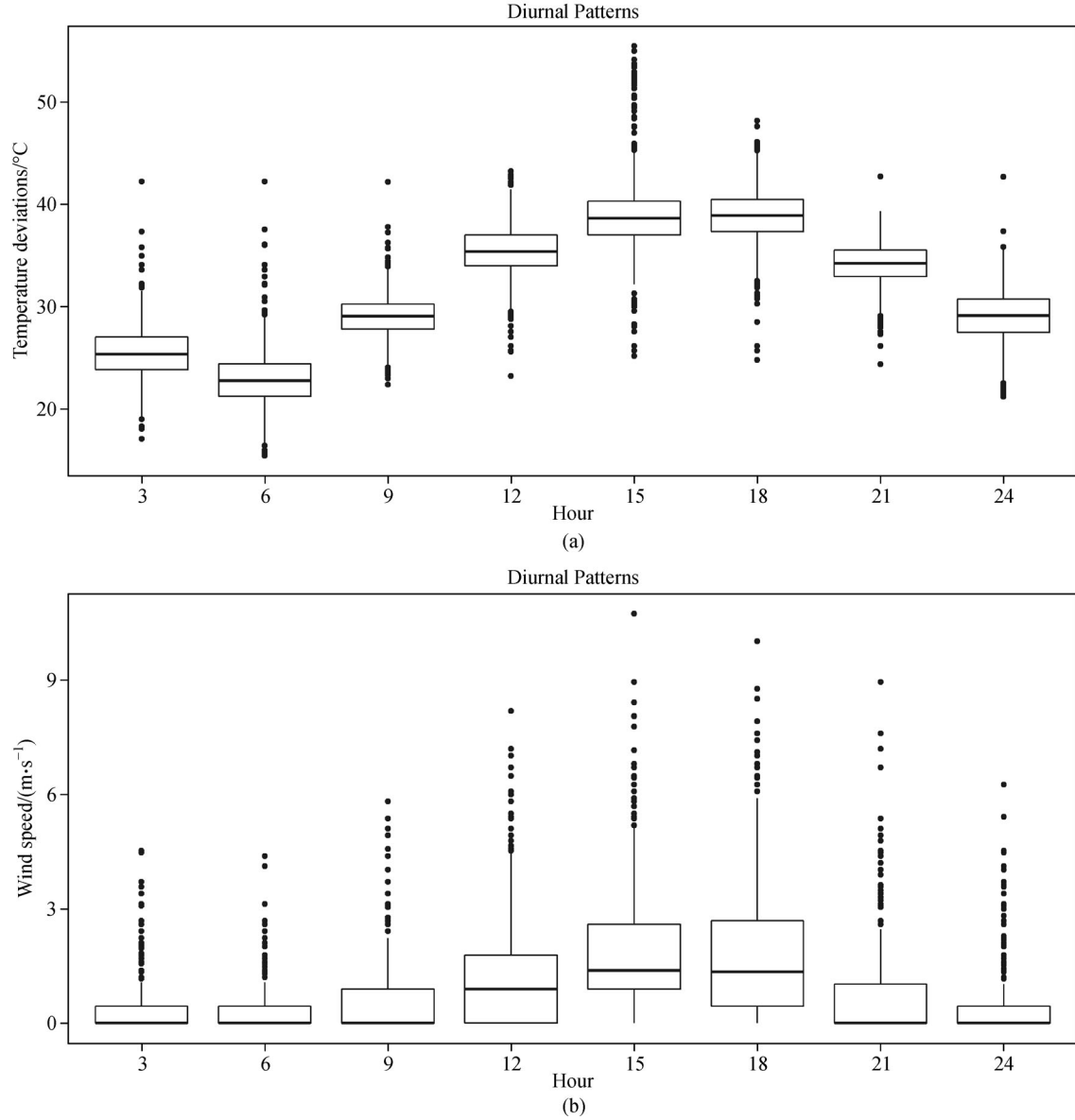It is remarkable, that although their presence was

Fig. 4 (a) Distributions of de-trended temperatures across 44 measurement locations. (b) Diurnal pattern of hourly averaged wind speed (in meters per second) measured at 44 weather stations during June, 2011.

prioritized in the model building procedure, predictors related to landscape composition are not statistically significant in LMM that correspond to different spatial aggregation levels (Tables 2–4). On the other hand, the patch density of soil is a significant configuration predictor in LMM_{50} (Table 3); as PD3 increases, the number of soil patches increases, negatively correlated with afternoon temperatures (Fig. 7). By adding PD3, however, the predictive performance of LMM_{50} in terms of MedAE, did not improve relative to LMM_{geog}. For higher levels of spatial aggregation ($r > 50$ m), the fractal dimension of buildings (FRAC1) is a strongly significant predictor for all LMM (Tables 3–4). This covariate is negatively correlated with nighttime temperatures (Fig. 7); hence,

more complex shaped buildings are associated with lower temperatures. LMM_{comb} is based on the fractal dimension of buildings calculated using spatial aggregation level of 350 m; the association of near-surface air temperatures with the fractal dimension of buildings manifests itself more strongly at this level of spatial aggregation.

The estimated negative effect of FRAC1 in LMM_{comb} appears stronger than the standardized effect of elevation (Table 2). In addition, incorporating FRAC1 into the model building process improves slightly the predictive ability of mixed-effects models (Fig. 8). On the other hand, given information on the fractal dimension of buildings, the patch density of soil ($r = 50$), which is positively associated with FRAC1 (the corresponding Spearman's correlation
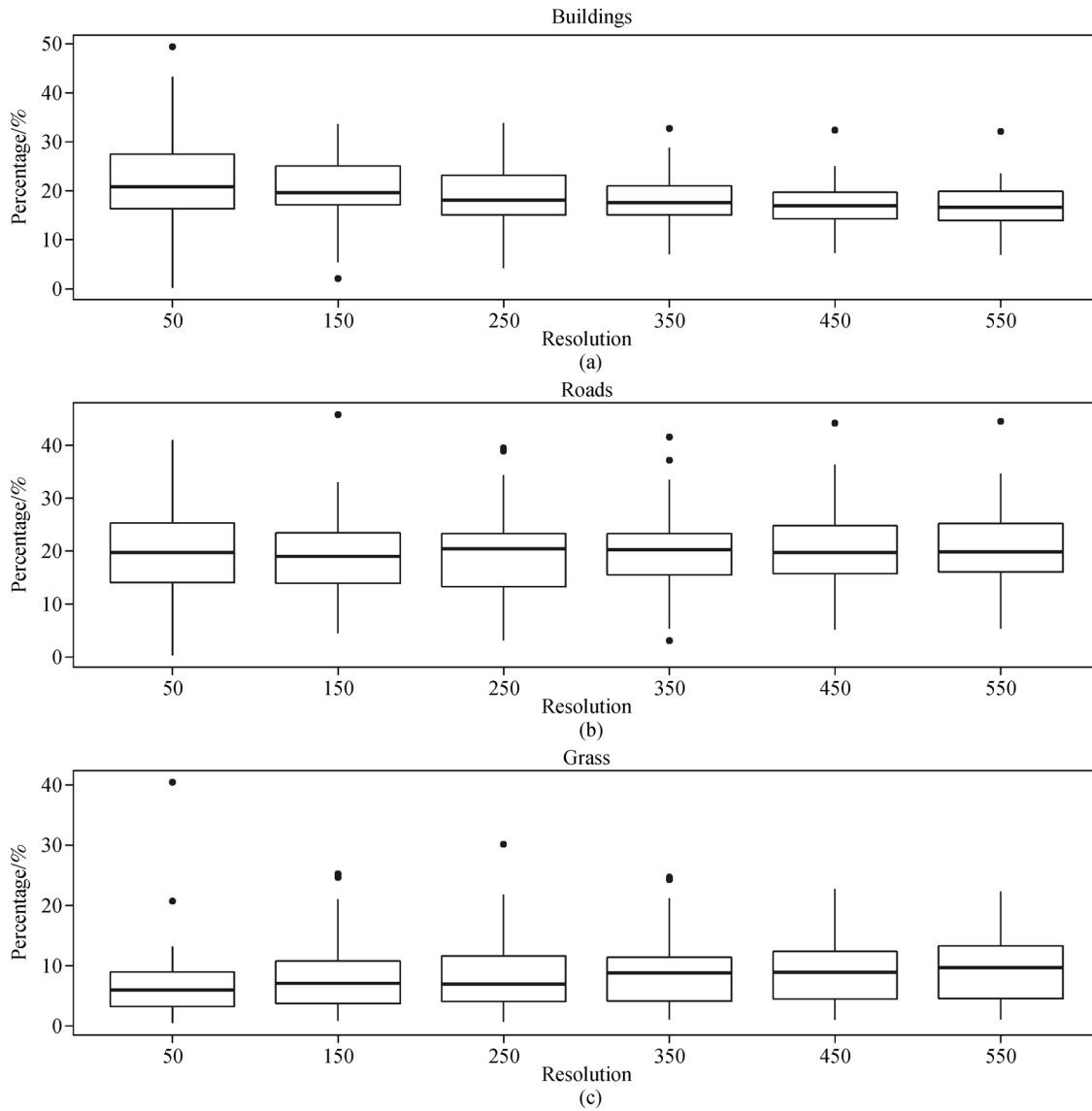
Fig. 5 Distributions of the percentage of buildings (a), roads (b) and grass (c) across measurement sites, for different levels of spatial aggregation.

coefficient equals 0.51), is not a significant predictor in LMM_{comb}. Hence, LMM_{comb} coincides with LMM_{350}. Compared to the null model LMM_0, which is based solely on temporal information, LMM_{comb} including predictors related to geographic information and landscape configuration achieves improved generalization ability and reduced uncertainty regarding the random effects that correspond to nighttime temperatures.

3.3 Relationship of air temperature and land configuration

The complexity of shape and level of patch density of different land covers (patches) of residential parcels help to reduce near-surface temperature, especially at night, apparently providing more variability in thermal diffusivity, increasing natural ventilation, and mitigating heat

storage (Cao et al., 2010; Connors et al., 2013). The increased complexity of the configuration of buildings, in this case residential houses, appears to be significantly and negatively associated with late night-early morning and late afternoon-early evening temperatures, respectively. A rationale for the late night-early morning result is not clear to us, but could be due to ventilation increases. The late afternoon-early evening result, during a period known as the evening transition (in temperature) suggests that complexly shaped homes provide multiple shaded spaces. In general, the larger the residential unit, the more complex the shape. The link between building shape and temperature, however, is not related to housing size measured by spatial area because in the analyzed data, PLAND1 is actually negatively correlated with FRAC1 (Spearman's correlation metric equals –0.41 at 350 m). While perhaps
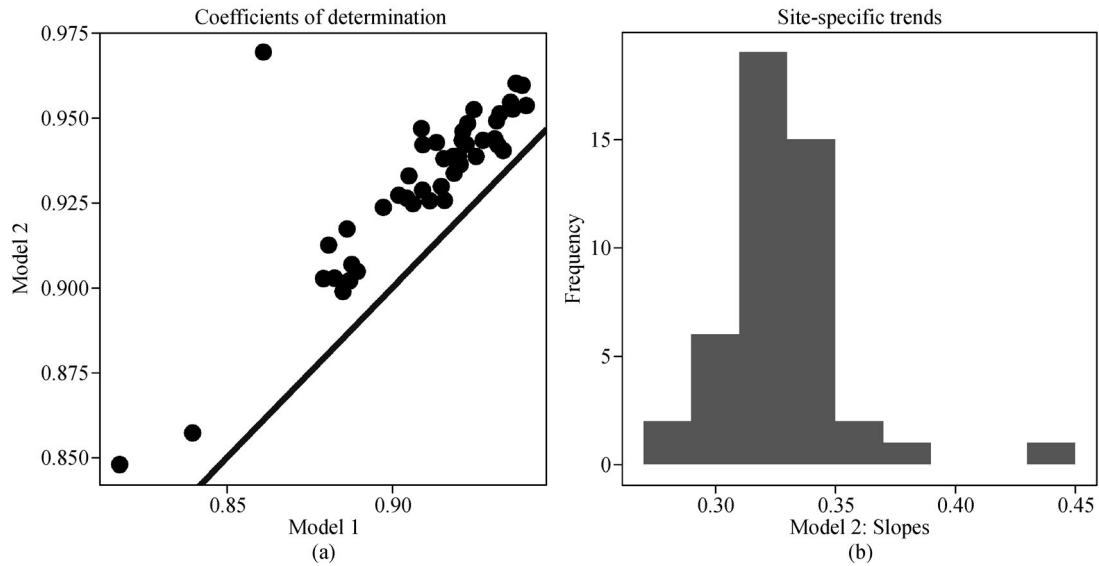
Fig. 6 (a) Coefficients of determination (R2) for site-specific regression models; Model 1 versus Model 2. (b) Site-specific slopes of the linear trends in Model 2.

surprising, the conservative modeling strategy employed, which requires strong evidence against the null hypothesis of non-significant effects of land configuration variables, indicates the strength of building shape-air temperature relationship.

Of the land-cover components examined, increased patch density and complexity of shape of the bare soil of desert-scaping and vegetation, both are negatively correlated with nighttime near-surface air temperatures. This result, also reported for land surface temperature studies in Phoenix (Myint et al., 2015; Li et al., 2017), follows from the influence of air movement across different densities and shapes of land cover units. A negative drop in temperature with increased patches, and not uniform large areas of soil, suggests that other land covers intervene to promote cooling – this is a point made for buildings (Connors et al., 2013). Interestingly, the shape of impervious surfaces had the weakest association with temperature, despite the well-known impacts of such surfaces on land surface temperature (Myint et al., 2013), perhaps reflecting the uniformity of roads, the principal factor in this land class. As expected, however, sensible heating from roads due to the lower albedo of asphalt (primarily) and anthropogenic emissions from moving vehicles, generates a significant positive correlation between the percentage area covered by roads and near-ground air temperature. Somewhat unexpected, no significant effect associated with predictors of vegetation was found during the day; this despite the considerable evidence for the cooling impacts of vegetation on land surface temperature (Myint et al., 2010; Chow et al., 2011; Jenerette et al., 2011; Declet-Barreto et al., 2013).

Finally, in contrast with previous studies, such as Li

et al. (2017), none of the predictors related to land composition were included in the final specifications, even though the model building process prioritized them. It should be emphasized, however, that the outcomes of this work do not suggest that land composition is not causally associated with temperatures. Although rich in terms of their temporal dimension relative to Li et al. (2017), the dataset analyzed here addresses a smaller number of sites. As a result, the statistical models can only identify the most prominent features of the association between land architecture and near-ground air temperatures.

Overall, our results are consistent with our broad hypothesis, generated from studies of land surface temperature (Myint et al., 2015; Li et al., 2016, 2017) that fine resolution, land-cover configuration has important, if incompletely identified, impacts on daytime and nighttime temperatures in the Phoenix metropolitan area. Interestingly, however, this study did not identify some of the more dominant attributes of land system architecture found for land surface temperature, such as the pattern and shape of vegetation cover. Rather, and surprisingly, metrics of building (residential homes) shape proved to be important in lowering temperatures during various parts of the daytime and nighttime. The degree to which the differences in the land architecture-temperature relationships reported in this and the former studies resides in temperature addressed, either land surface or near-ground, has yet to be determined.

3.4 Limitations

Perhaps the most important limitation in this study is the use of WeatherUnderground (WU) data from residences in
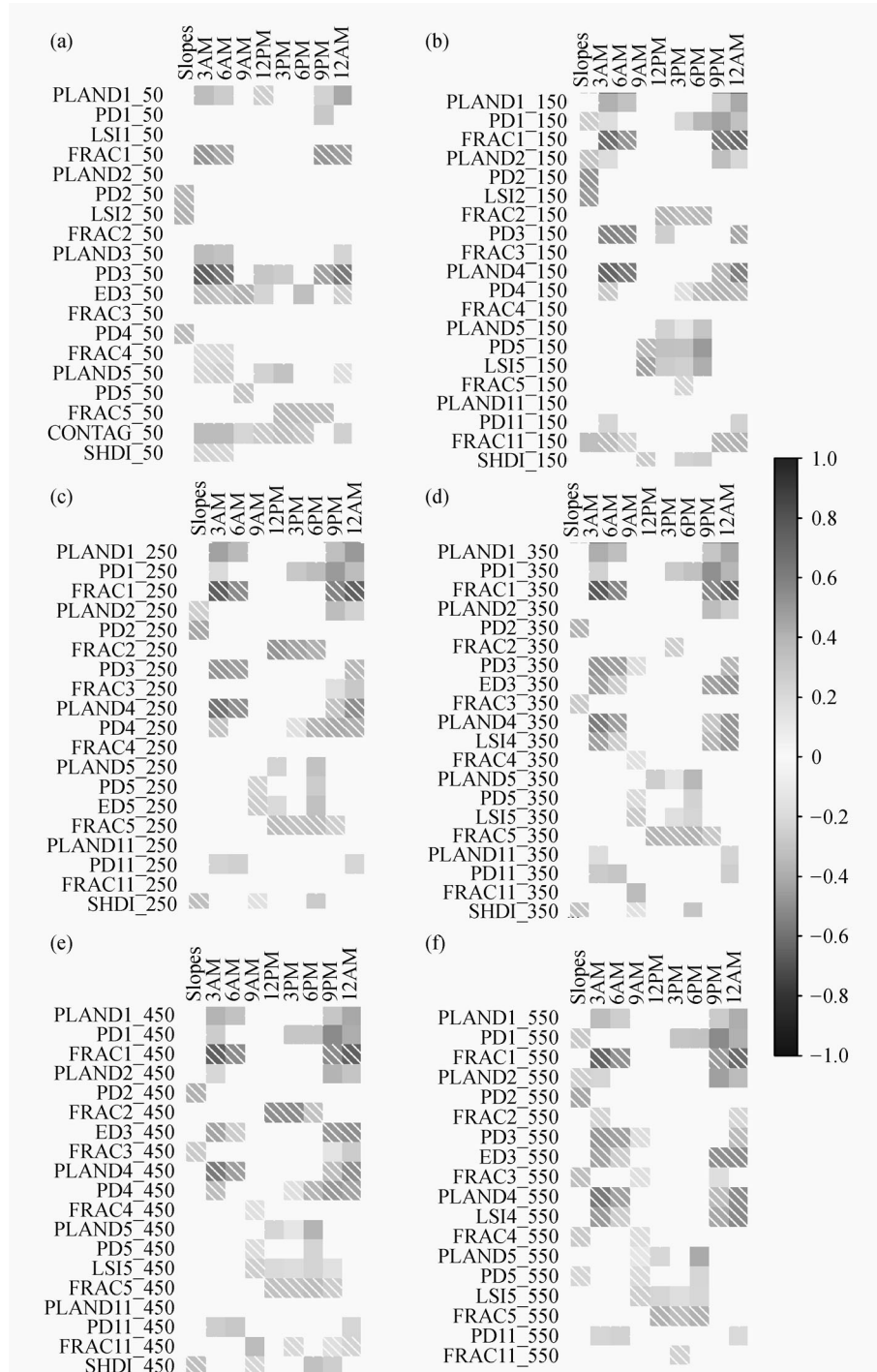
Fig. 7 Pearson's correlations of the parameters in site-specific models (2) with land system architecture metrics. Plots correspond to different levels of spatial aggregation (a) 50 m; (b) 150 m; (c) 250 m; (d) 350 m; (e) 450 m; (f) 550 m. Darker tones represent stronger linear associations; solid squares depict positive correlations. Correlations which are not significant at the 0.01 level are not displayed. Land architecture metrics in each plot were selected using a backward stepwise procedure based on VIF. Land cover classes are designated as follows. 1: Buildings, 2: Roads, 3: Soil, 4: Trees/Shrubs, 5: Grass and 11: Pools.
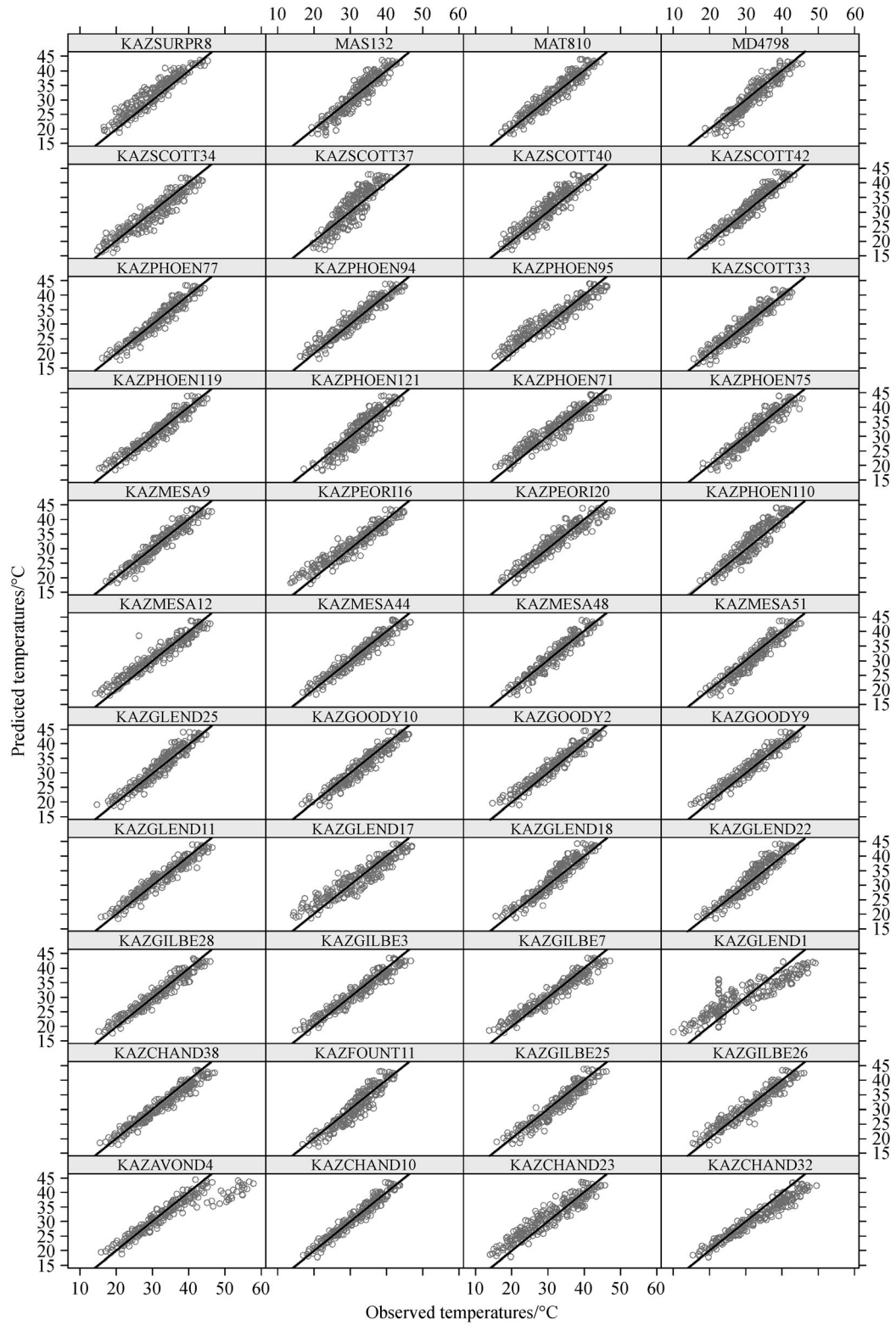
Fig. 8 Observed versus predicted near surface temperatures: leave-one-site cross-validation based on LMM_{comb}.

Table 2 Estimated mixed-effects models LMM$_0$, LMM$_{geog}$, LMM$_{comb}$, for air temperatures. Fixed effects coefficients are significant with $p < 0.01$. Standard deviations of significant random effects are shown in parentheses, next to the corresponding fixed-effects coefficients. Land cover classes are designated as follows. 1: Buildings, 2: Roads, 3: Soil, 4: Trees/Shrubs, 5: Grass

Variable	LMM$_0$		LMM$_{geog}$		LMM$_{comb}$	
	Coefficient	Std Error	Coefficient	Std Error	Coefficient	Std Error
12AM	28.956 (1.454)	0.234	28.956 (1.450)	0.233	28.959 (1.174)	0.185
3AM	25.275 (1.341)	0.223	25.276 (1.447)	0.223	25.279 (1.158)	0.183
6AM	22.563 (1.333)	0.241	22.564 (1.550)	0.241	22.566 (1.286)	0.201
9AM	28.898 (1.358)	0.23	28.898 (1.489)	0.23	28.901 (1.539)	0.238
12PM	35.506 (1.427)	0.204	35.507 (1.253)	0.202	35.510 (1.453)	0.226
3PM	38.928 (2.371)	0.332	38.929 (2.176)	0.332	38.931 (2.239)	0.342
6PM	39.005 (1.455)	0.191	39.006 (1.187)	0.191	39.008 (1.347)	0.21
9PM	34.101 (1.226)	0.171	34.101 (1.069)	0.17	34.103 (0.976)	0.157
Lin. Trend	2.733	0.043	2.733	0.043	2.733	0.043
Elevation			−0.496	0.085	−0.223	0.089
FRAC1_350					−0.485	0.088
ME/°C	0.015		0.007		−0.007	
MedAE/°C	1.583		1.555		1.554	
RMSE/°C	2.301		2.268		2.256	

Table 3 Estimated mixed-effects models LMM$_{50}$, LMM$_{150}$, LMM$_{250}$, for air temperatures. Fixed effects coefficients are significant with $p < 0.01$. Standard deviations of significant random effects are shown in parentheses, next to the corresponding fixed-effects coefficients. Land cover classes are designated as follows. 1: Buildings, 2: Roads, 3: Soil, 4: Trees/Shrubs, 5: Grass

Variable	LMM$_{50}$		LMM$_{150}$		LMM$_{250}$	
	Coefficient	Std Error	Coefficient	Std Error	Coefficient	Std Error
12AM	28.959 (1.311)	0.205	28.959 (1.259)	0.189	28.959 (1.201)	0.189
3AM	25.278 (1.297)	0.203	25.278 (1.243)	0.187	25.279 (1.189)	0.187
6AM	22.566 (1.411)	0.219	22.566 (1.359)	0.205	22.566 (1.315)	0.205
9AM	28.901 (1.450)	0.225	28.901 (1.531)	0.237	28.901 (1.533)	0.237
12PM	35.509 (1.366)	0.213	35.509 (1.398)	0.224	35.509 (1.441)	0.224
3PM	38.931 (2.248)	0.343	38.931 (2.203)	0.341	38.931 (2.235)	0.341
6PM	39.008 (1.241)	0.195	39.008 (1.278)	0.208	39.008 (1.329)	0.208
9PM	34.103 (0.981)	0.157	34.103 (0.973)	0.156	34.103 (0.968)	0.156
Lin. Trend	2.733	0.042	2.733	0.043	2.733	0.043
Elevation	−0.478	0.083	−0.283	0.09	−0.237	0.09
PD3_50	−0.308	0.083				
FRAC1_150			−0.386	0.09		
FRAC1_250					−0.450	0.089
ME/°C	−0.009		−0.008		−0.007	
MedAE/°C	1.561		1.553		1.554	
RMSE/°C	2.263		2.258		2.256	

the Phoenix metropolitan area. WU provides standardized weather monitoring stations that report observations directly to the organization and made public. Geographical coordinates provide the capacity to match the stations to their parcels. The precise positioning of the station (e.g., height above the ground and shade conditions) is lacking,

Table 4   Estimated mixed-effects models LMM$_{350}$, LMM$_{450}$, LMM$_{550}$, for air temperatures. Fixed effects coefficients are significant with $p < 0.01$. Standard deviations of significant random effects are shown in parentheses, next to the corresponding fixed-effects coefficients. Land cover classes are designated as follows. 1: Buildings, 2: Roads, 3: Soil, 4: Trees/Shrubs, 5: Grass

Variable	LMM$_{350}$		LMM$_{450}$		LMM$_{550}$	
	Coefficient	Std Error	Coefficient	Std Error	Coefficient	Std Error
12AM	28.959 (1.174)	0.185	28.959 (1.188)	0.187	28.959 (1.223)	0.192
3AM	25.279 (1.158)	0.183	25.278 (1.175)	0.185	25.278 (1.210)	0.19
6AM	22.566 (1.286)	0.201	22.566 (1.303)	0.204	22.566 (1.333)	0.208
9AM	28.901 (1.539)	0.238	28.901 (1.530)	0.237	28.900 (1.516)	0.235
12PM	35.510 (1.453)	0.226	35.509 (1.437)	0.223	35.509 (1.410)	0.219
3PM	38.931 (2.239)	0.342	38.931 (2.228)	0.34	38.931 (2.215)	0.338
6PM	39.008 (1.347)	0.21	39.008 (1.332)	0.208	39.008 (1.309)	0.205
9PM	34.103 (0.976)	0.157	34.103 (0.985)	0.158	34.103 (1.001)	0.16
Lin. Trend	2.733	0.043	2.733	0.043	2.734	0.043
Elevation	−0.223	0.089	−0.235	0.089	−0.266	0.089
FRAC1_350	−0.485	0.088				
FRAC1_450			−0.467	0.089		
FRAC1_550					−0.418	0.089
ME/°C	−0.007		−0.006		−0.004	
MedAE/°C	1.554		1.552		1.559	
RMSE/°C	2.256		2.257		2.258	

however, and this positioning can affect the temperatures recorded. We could not control for station positions but assume that the 44 stations were relatively equally distributed among similar parcel positions.

In addition, we explore only one month, as opposed to a full year. In doing so, we fully recognize that the relationships revealed in this study may change by season or by the addition of later summer months. One study that considered seasonal land surface temperature in the Phoenix area indicates the impacts of land-cover composition and, perhaps, configuration have varied summer to winter (Myint et al., 2013), which may be related to hysteresis effects between surface and air temperature (Song et al., 2017). Elaboration of seasonal impacts of land architecture on residential air temperature in the Phoenix area awaits further study. Our attention to June was fostered by the overwhelming concern in the Phoenix metropolitan area of extreme summer heat, which becomes common in June, and the various means to mitigate it, including attention to land cover (City of Phoenix). To standardize daily weather conditions as much as possible, we eliminated the more volatile conditions of July and August, triggered by monsoon precipitation and winds, because their addition would likely yield much more complex results.

Ninety percent of the NAIP data used to determine land-cover characteristics correspond to a five-day period in early June, 2010, whereas the temperature data were collected in June, 2011. Two dates in August and September 2010 correspond to 10% of the NAIP data. Our assumption is that the vast majority of the land covers present in 2010 were present in 2011 as well. In addition, while our selected parcels were single family residential in kind, in some cases the larger radii assessments may have overlapped into non-residential parcels such as parking lots or parks, affecting the calculations of land-cover composition and configuration. Finally, this study did not explore metrics of land-cover pattern and shape other than FRAGSTATS.

Our urban canopy level air temperature LMM error measures of ME, MedAE, and RMSE may relate to many of the above issues, but are close to error measures reported by other urban climate researchers addressing Phoenix at micro-scales, who use sophisticated numerical models (Chow and Brazel, 2012; Middel et al., 2014). Error measure values reported in many studies are derived typically by comparing model predictions, with ground level or above roof level weather station data. For the most part, the weather locales used in most of these studies are commonly sited over relatively uniform surface conditions or source areas within close proximity of the stations. For example, Grossman-Clarke et al. (2010) applied a physics-based complex Weather Research and Forecasting Model (WRF) in conjunction with the Noah Urban Canopy Model (UCM) at a resolution of 2 km and Landsat data (30 m pixels) categorized into 12 LULC types. This study

conducted for Phoenix resulted in reported RMSE of 1°C–3°C for daytime and upwards of 5°C at night between model air temperatures and weather site values. Georgescu et al. (2011), averaging data across 8 urban and rural ground sites yielded better agreement with similar modeling approach (~0.6°C to 1.3°C). Research using WRF UCM modeling techniques applied to Tokyo, Osaka and Nagoya metropolitan areas by Kusaka et al. (2012) yielded a reported RMSE of a similar magnitude to our statistical approach (ca. 2.7°C). RMSE errors reported by Loridan et al. (2013) range from 1.3°C to 1.6°C, however, in that study temperature data from instrumented towers are used at heights above the urban canopy level where there would be less heterogeneity across space. Errors for finer scale microclimate models may not be any different. Chow and Brazel (2012) and Middel et al. (2014), for example, used a high resolution version of the ENVI met model in east valley residence locations of the Phoenix metro area and compared output to onsite weather stations with RMSE results ranging from 1.4°C–3.0°C.

The above-mentioned errors, especially in comparison to urban canopy air temperatures, may significantly relate to what is evaluated in the international urban energy balance model comparison study of Grimmond et al. (2011). Energy balance experiments tested 33 urban climate models that showed higher errors occur in most models for the turbulent and latent heat fluxes in urban areas than other components of the urban energy balance. These flux errors directly affect predictions of temperatures and would tend to explain what appear to be high RMSEs in estimating urban canopy air temperatures.

4   Concluding remarks

Incipient research on "urban-scapes" through the lens of fine-resolution land system architecture approaches is underway. It demonstrates that both the composition and the configuration of land covers, foremost in terms of their patterns, affect land surface temperature, especially for desert cities, such as Phoenix, AZ (Zhou et al., 2011; Li et al., 2012; Connors et al., 2013; Myint et al., 2015; Zhang et al., 2017). Increasingly, configuration in terms of land-cover shape has been shown to influence land surface temperature as well (Maimaitiyiming et al., 2014; Huang and Cadenasso, 2016; Li et al., 2016, 2017). That these direct surface-temperature relationships uncovered at such fine spatial resolution extend to near-ground temperatures has been less explored.

This study advances this exploration by examining fine-resolution land-cover configuration impacts on near-ground air temperature for 44 residential neighborhoods in the Phoenix, AZ, metroplex, for the month of June, 2011. It indicates that complex single-family (residence) building shapes are associated with lower air temperatures and the optimal level of spatial aggregation for identifying

this association is 350 m. The patch density of soil is weakly and negatively associated with nighttime air temperatures, but this relationship is identified only at the finer level of spatial aggregation (50 m). The building shape impact is surprising, as it has not emerged strongly in the literature linked to land system architecture to date.

While preliminary in nature and in need of expansion to larger datasets for further analysis, our study indicates that this relationship requires further examination. Our results, coupled with those from research on land surface temperature, suggests that the configuration of land covers of residential parcels in the Phoenix area affects temperature sufficiently that further exploration of fine-resolution, land system architecture is warranted. They also point to the design of land covers from the parcel level to the metroplex at large, as a means to address extreme temperatures and the dis-services associated with them in desert cities.

References

Akbari H, Matthews H D (2012). Global cooling updates: reflective roofs and pavements. Energy Build, 55: 2–6

Akbari H, Pomerantz M, Taha H (2001). Cool surfaces and shade trees to reduce energy use and improve air quality in urban areas. Sol Energy, 70(3): 295–310

Baker L A, Brazel A J, Selover N, Martin C, McIntyre N, Steiner F R, Nelson A, Musacchio L (2002). Urbanization and warming of Phoenix (Arizona, USA): impacts, feedbacks and mitigation. Urban Ecosyst, 6(3): 183–203

Bowler D E, Buyung-Ali L, Knight T M, Pullin A S (2010). Urban greening to cool towns and cities: a systematic review of the empirical evidence. Landsc Urban Plan, 97(3): 147–155

Brazel A, Gober P, Lee S J, Grossman-Clarke S, Zehnder J, Hedquist B, Comparri E (2007). Determinants of changes in the regional urban heat island in metropolitan Phoenix (Arizona, USA) between 1990 and 2004. Clim Res, 33(2): 171–182

Brazel A, Selover N, Vose R, Heisler G (2000). The tale of two climates—Baltimore and Phoenix urban LTER sites. Clim Res, 15(2): 123–135

Cao X, Onishi A, Chen J, Imura H (2010). Quantifying the cool island intensity of urban parks using ASTER and IKONOS data. Landsc Urban Plan, 96(4): 224–231

Cermak V, Bodri L, Kresl M, Dedecek P, Safanda J (2017). Eleven years of ground-air temperature tracking over different land cover types. Int J Climatol, 37(2): 1084–1099

Chow W T L, Brazel A (2012). Assessing xeriscaping as a sustainable heat island mitigation approach for a desert city. Build Environ, 47: 170–181

Chow W T L, Brennan D, Brazel A (2012). Urban heat island research in Phoenix, Arizona: theoretical contributions and policy applications. Bull Am Meteorol Soc, 93(4): 517–530

Chow W T L, Pope R L, Martin C A, Brazel A (2011). Observing and modeling the nocturnal park cool island of an arid city: horizontal and vertical impacts. Theor Appl Climatol, 103(1–2): 197–211

Chow W T L, Svoma B M (2011). Analyses of nocturnal temperature cooling-rate response to historical local-scale urban land-use/land cover change. J Appl Meteorol Climatol, 50(9): 1872–1883

Chow W T L, Volo T J, Vivoni E R, Jenerette D G, Ruddell B L (2014). Seasonal dynamics of a suburban energy balance in Phoenix, Arizona. Int J Climatol, 34(15): 3863–3880

Connors J P, Galletti C S, Chow W T (2013). Landscape configuration and urban heat island effects: assessing the relationship between landscape characteristics and land surface temperature in Phoenix, Arizona. Landsc Ecol, 28(2): 271–283

Declet-Barreto J, Brazel A, Martin C A, Chow W T, Harlan S L (2013). Creating the park cool island in an inner-city neighborhood: heat mitigation strategy for Phoenix, AZ. Urban Ecosyst, 16(3): 617–635

Faeth S H, Bang C, Saari S (2011). Urban biodiversity: patterns and mechanisms. Ann N Y Acad Sci, 1223(1): 69–81

Fast J D, Torcolini J C, Redman R (2005). Pseudovertical temperature profiles and the urban heat island measured by a temperature datalogger network in Phoenix, Arizona. J Appl Meteorol, 44(1): 3–13

Forman R T T (1990). Ecologically sustainable landscapes: the role of spatial configuration. In: Forman R T T, Zonnelfeld I S, eds. Changing Landscapes: An Ecological Perspective. New York: Springer, 261–278

Georgescu M, Morefield P E, Bierwagen B G, Weaver C P (2014). Urban adaptation can roll back warming of emerging megapolitan regions. Proc Natl Acad Sci USA, 111(8): 2909–2914

Georgescu M, Moustaoui M, Mahalov A, Dudhia J (2011). An alternative explanation of the semiarid urban area "oasis effect". J Geophys Res, 116(D24): D24113

Gill S E, Handley J F, Ennos A R, Pauleit S (2007). Adapting cities for climate change: the role of the green infrastructure. Built Environ, 33 (1): 115–133

Gober P, Kirkwood C W, Balling R C, Ellis A W, Deitrick S (2010). Water planning under climatic uncertainty in Phoenix: Why we need a new paradigm? Ann Assoc Am Geogr, 100(2): 356–372

Grimmond C S B, Blackett M, Best M J, Baik J J, Belcher S E, Beringer J, Bohnenstengel S I, Calmet I, Chen F, Coutts A, Dandou A, Fortuniak K, Gouvea M L, Hamdi R, Hendry M, Kanda M, Kawai T, Kawamoto Y, Kondo H, Krayenhoff E S, Lee S H, Loridan T, Martilli A, Masson V, Miao S, Oleson K, Ooka R, Pigeon G, Porson A, Ryu Y H, Salamanca F, Steeneveld G J, Tombrou M, Voogt J A, Young D T, Zhang N (2011). Initial results from Phase 2 of the international urban energy balance model comparison. Int J Climatol, 31(2): 244–272

Grimmond S (2007). Urbanization and global environmental change: local effects of urban warming. Geogr J, 173(1): 83–88

Grossman-Clarke S, Zehnder J A, Loridan T L, Grimmond S B (2010).

Contribution of land uses changes to near-surface air temperature during recent summer extreme heat events in the Phoenix metropolitan area. American Meteorological Society, 49(8): 1649–1664

Guhathakurta S, Gober P (2010). Residential land use, the urban heat island, and water use in Phoenix: a path analysis. J Plann Educ Res, 30(1): 40–51

Harlan S, Brazel A, Prashad L, Stefanov W L, Larsen L (2006). Neighborhood microclimates and vulnerability to heat stress. Soc Sci Med, 63(11): 2847–2863

Hondula D M, Vanos J K, Gosling S N (2013). The SSC: a decade of climate–health research and future directions. Int J Biometeorol, 58 (2): 1–12

Huang G, Cadenasso M L (2016). People, landscape, and urban heat island: dynamics among neighborhood social conditions, land cover and surface temperatures. Landsc Ecol, 31(10): 2507–2515

Jacobson M Z, Ten Hoeve J E (2012). Effects of urban surface and white roofs on global and regional climate. J Clim, 25(3): 1028–1044

James G, Witten D, Hastie T, Tibshirani R (2013). An Introduction to Statistical Learning. New York: Springer

Jenerette G D, Harlan S, Buyantuev A, Stefanov W L, Declet-Barreto J, Ruddell B L, Myint S, Kaplan S, Li X (2016). Micro-scale urban surface temperatures are related to land-cover features and residential heat related health impacts in Phoenix, AZ USA. Landsc Ecol, 31(4): 745–760

Jenerette G D, Harlan S, Stefanov W L, Martin C A (2011). Ecosystem services and urban heat riskscape moderation: water, green spaces, and social inequality in Phoenix, USA. Ecol Appl, 21(7): 2637–2651

Krüger E L, Minella F O, Rasia F (2011). Impact of urban geometry on outdoor thermal comfort and air quality from field measurements in Curitiba, Brazil. Build Environ, 46(3): 621–634

Kusaka H, Hara M, Takane Y (2012). Urban climate projection by the WRF Model at 3-km horizontal grid increment: dynamical down-scaling and predicting heat stress in the 2070s August for Tokyo, Osaka, and Nagoya, metropolises. J Meteorol Soc Jpn, 90B(0): 47–63

Li J, Song C, Cao L, Zhu F, Meng X, Wu J (2011). Impacts of landscape structure on surface urban heat islands: a case study of Shanghai, China. Remote Sens Environ, 115(12): 3249–3263

Li X, Kamarianakis Y, Ouyang Y, Turner B L II, Brazel A (2017). On the association between land system architecture and land surface temperatures: evidence from a desert metropolis—Phoenix, Arizona, U.S.A. Landsc Urban Plan, 163: 107–120

Li X, Li W, Middel A, Harlan S L, Brazel A, Turner B L II (2016). Remote sensing of the surface urban heat island and land architecture in Phoenix, Arizona: combined effects of land composition and configuration and cadastral-demographic-economic factors. Remote Sens Environ, 174: 233–243

Li X, Myint S, Zhang Y, Galletti C, Zhang X, Turner B L II (2014). Object-based land-cover classification for metropolitan Phoenix, Arizona, using aerial photography. Int J Appl Earth Obs Geoinf, 33: 321–330

Li X, Zhou W, Ouyang Z, Xu W, Zheng H (2012). Spatial pattern of greenspace affects land surface temperature: evidence from the heavily urbanized Beijing metropolitan area China. Landsc Ecol, 27 (6): 887–898

Lindén J (2011). Nocturnal cool island in the Sahelian city of Ouagadougou, Burkina Faso. Int J Climatol, 31(4): 605–620

Loridan T, Lindberg F, Jorba O, Kotthaus S, Grossman-Clarke S, Grimmond C S B (2013). High resolution simulation of the variability of surface energy balance fluxes across Central London with urban zones for energy partitioning. Boundary-Layer Meteorol, 147(3): 493–523

Maimaitiyiming M, Ghulam A, Tiyip T, Pla F, Latorre-Carmona P, Halik Ü, Sawut M, Caetano M (2014). Effects of green space spatial pattern on land surface temperature: implications for sustainable urban planning and climate change adaptation. ISPRS J Photogramm Remote Sens, 89: 59–66

McGarigal K, Cushman S A, Ene E (2012). FRAGSTATS v4: Spatial Pattern Analysis Program for Categorical and Continuous Maps. University of Massachusetts, Amherst, MA

Middel A, Brazel A, Kaplan S, Myint S (2012). Daytime cooling efficiency and diurnal energy balance in Phoenix, Arizona, USA. Clim Res, 54(1): 21–34

Middel A, Häb K, Brazel A J, Martin C A, Guhathakurta S (2014). Impact of urban form and design on mid-afternoon microclimate in Phoenix Local Climate Zones. Landsc Urban Plan, 122: 16–28

Myint S W, Zheng B, Talen E, Fan C, Kaplan S, Middel A, Smith M, Huang H P, Brazel A (2015). Does the spatial arrangement of urban landscape matter? Examples of urban warming and cooling in Phoenix and Las Vegas. Ecosyst Health Sustain, 1(4): 1–15

Myint S, Brazel A, Okin G, Buyantuyev A (2010). Combined effects of impervious surface and vegetation cover on air temperature variations in a rapidly expanding desert city. GIsci Remote Sens, 47(3): 301–320

Myint S, Wentz E A, Brazel A, Quattrochi D A (2013). The impact of distinct anthropogenic and vegetation features on urban warming. Landsc Ecol, 28(5): 959–978

Nichol J E, Fung W Y, Lam K, Wong M S (2009). Urban heat island diagnosis using ASTER satellite images and 'in situ' air temperature. Atmos Res, 94(2): 276–284

Oke T R (2006). Initial guidance to obtain representative meteorological observations at urban sites. In: IOM Report No. 81. WMO/TD No. 1250. Geneva: World Meteorological Organization

Pinheiro J C, Bates D M (2009). Mixed Effects Models in S and S-plus. New York: Springer

Song J, Wang Z H, Myint S W, Wang C (2017). The hysteresis effect on surface-air temperature relationship and its implications to urban planning: an examination in Phoenix, Arizona, USA. Landsc Urban Plan, 167: 198–211

Stewart I D, Oke T R (2012). Local climate zones for urban temperature studies. Bull Am Meteorol Soc, 93(12): 1879–1900

Stewart I D, Oke T R, Krayenhoff E S (2014). Evaluation of the 'local climate zone' scheme using temperature observations and model simulations. Int J Climatol, 34(4): 1062–1080

Stewart J Q, Whiteman C D, Steenburgh W J, Bian X (2002). A climatological study of thermally driven wind systems of the U. S. intermountain west. Bull Am Meteorol Soc, 83(5): 699–708

Stoll M J, Brazel A J (1992). Surface-air temperature relationships in the urban environment of Phoenix, Arizona. Phys Geogr, 13(2): 160–179

Stone B Jr, Rodgers M O (2001). Urban form and thermal efficiency: how the design of cities influences the urban heat island effect. J Am Plann Assoc, 67(2): 186–198

Turner B L II (2016). Land system architecture for urban sustainability: new directions for land system science illustrated by application to the urban heat island problem. J Land Use Sci, 11(6): 689–697

Turner B L II, Janetos A C, Verburg P H, Murray A T (2013). Land system architecture: using land systems to adapt and mitigate global environmental change. Glob Environ Change, 23(2): 395–397

Voogt J A, Oke T R (2003). Thermal remote sensing of urban climates. Remote Sens Environ, 86(3): 370–384

Wang Y, Akbari H (2016). Analysis of urban heat island phenomenon and mitigation solutions evaluations for Montreal. Sustainable Cities and Society, 26: 438–446

Wentz E A, Stefanov W L, Gries C, Hope D (2006). Land use and land cover mapping from diverse data sources for an arid urban environments. Comput Environ Urban Syst, 30(3): 320–346

Wong N H, Yu C (2005). Study of green areas and urban heat island in a tropical city. Habitat Int, 29(3): 547–558

Xiao R, Ouyang Z, Zheng H, Li W, Schienke E W, Wang X (2007). Spatial pattern of impervious surfaces and their impacts on land surface temperature in Beijing, China. J Environ Sci (China), 19(2): 250–256

Yang F, Lau S Y, Qian F (2011). Urban design to lower summertime outdoor temperatures: an empirical study on high-rise housing in Shanghai. Build Environ, 46(3): 769–785

Zhang Y, Murray A, Turner B L II (2017). Optimizing green space locations to reduce daytime and nighttime urban heat island effects in Phoenix, Arizona. Landsc Urban Plan, 165: 162–171

Zhou W, Huang G, Cadenasso M L (2011). Does spatial configuration matter? Understanding the effects of land cover pattern on land surface temperature in urban landscapes. Landsc Urban Plan, 102(1): 54–63

Zuur A, Ieno E N, Walker N, Savaliev A A, Smith G M (2009). Mixed Effects Models and Extensions in Ecology with R. New York: Springer

Author Biographies

Yiannis KAMARIANAKIS received a PhD in mathematical economics and finance at the University of Crete, Greece in 2007, and a M.Sc. in Statistics and B.Sc. in Mathematics, respectively, at Athens University of Economics and Business, Athens in 2000 and University of Crete, Greece in 1998. He is an assistant professor at School of Mathematical and Statistical Sciences, Arizona State University (ASU). Before joining ASU he worked as a postdoctoral researcher at IBM Research and Cornell University. He is the author of more than 50 publications relating to applied statistical modeling, with an emphasis on environmental applications. E-mail: yiannis76@asu.edu

Xiaoxiao LI received a PhD in forestry and natural resources at Purdue University, Indiana in 2011, and a MA and BA, respectively, at Clark University, Massachusetts in 2005 and Zhejiang University, China in 2005. She is a research analyst working at School of Geographical Sciences and Urban Planning and Global Institute of

Sustainability, Arizona State University. She works on multiple resolution land-cover and land-use classifications for the Central Arizona-Phoenix Long-term Ecological Research program and examines impact of fine-resolution land system architecture on urban sustainability, foremost the urban heat island effect. E-mail: xiaoxia4@asu.edu

B. L. TURNER II   received a PhD in geography at the University of Wisconsin, Madison in 1974, and a MA and BA in geography in 1968 and 1969, respectively, at the University of Texas at Austin. He is the Gilbert F. White Professor of Environment and Society and Regent's Professor, School of Geographical Sciences and Urban Planning and School of Sustainability, Arizona State University. He is the author of more than 200 publications dealing with human-environment relationships, ranging from ancient Maya agriculture and environment in Mexico and Central America to contemporary global land-use change and sustainability science. Dr. Turner is member of the U.S. National Academy of Sciences and American Academy of Arts of Sciences, and serves as Associate Editor, Proceedings of the National Academy of Sciences, and on numerous national and international panels and committees addressing land change and sustainability science. E-mail: billie.l.turner@asu.edu

Anthony J. BRAZEL   received a PhD in geography at the University of Michigan in 1972 and an MA in geography (1965) and BA in Mathematics (1963), respectively, at Rutgers University. He is an Emeritus Professor in the School of Geographical Sciences & Urban Planning at Arizona State University. He served as governor-appointed State Climatologist for Arizona for 20 years and was elected Fellow of the American Association for the Advancement of Science for his early career research on ice and snow processes in high mountains. He is the recipient of the Climate Specialty Group Lifetime Achievement Award of the American Association of Geographers; The Helmut E. Landsberg Award on urban environ-ments from the American Meteorological Society; the Luke Howard Award from the International Association on Urban Climate; and the Jeffrey Cook Prize in Desert Architecture for urban climate research from the J. Blaustein Institutes for Desert Research, Ben-Gurion University of the Negev. Dr. Brazel has authored more than 200 publications on topics related to physical geography and boundary layer climate, ice and snow processes, and desert urban climatology. E-mail: abrazel@asu.edu